


ORIGINAL ARTICLE

Polybenzimidazole functionalized electrolyte with Li-wetting and self-fluorination functionalities for practical Li metal batteries

Dongjiang Chen^{1,2} | Yuanpeng Liu¹ | Chuan Xia³ | Yupei Han^{1,2} | Qingwei Sun^{1,2} | Xuchang Wang² | Wei Chen² | Xian Jian³ | Weiqiang Lv² | Jianyi Ma⁴ | Weidong He^{1,2} 

¹National Key Laboratory of Science and Technology on Advanced Composites in Special Environments, and Center for Composite Materials and Structures, Harbin Institute of Technology, Harbin, China

²School of Physics, University of Electronic Science and Technology of China, Chengdu, China

³School of Materials and Energy, University of Electronic Science and Technology of China, Chengdu, China

⁴Institute of Atomic and Molecular Physics, Sichuan University, Chengdu, Sichuan, China

Correspondence

Weidong He, National Key Laboratory of Science and Technology on Advanced Composites in Special Environments, and Center for Composite Materials and Structures, Harbin Institute of Technology, Harbin 150080, China.
Email: weidong.he@hit.edu.cn

Funding information

Applied Fundamental Research Fund of Sichuan Province, Grant/Award Number: 2019YJ0169; Fundamental Research Funds for the Chinese Central Universities, Grant/Award Number: ZYGX2015Z003; Natural Science Foundation of China, Grant/Award Number: 51972043; Science & Technology Support Funds of Sichuan Province, Grant/Award Number: 2016GZ0151

Abstract

Rough Li plating, low ionic conductivity, and low thermal stability of conventional electrolytes post-primary challenges for achieving reliable high-capacity rechargeable lithium batteries, for which lithium metal is frequently proposed as the most promising anode material. Conventional low-polarity commercial polypropylene/polyethylene separators fail to support the application of high-energy-density Li anodes due to their rigid physicochemical properties and the high reactivity of Li metal, leading to fatal dendrite formation and vigorous exothermic reaction with electrolytes. Herein, we develop a Li-wetting, flame-retardant binary polymer electrolyte by functionalizing poly(vinylidene fluoride) (PVDF) separators with non-flammable polybenzimidazole (PBI) to build safe room-temperature solid-state electrolyte membranes. A dendrite-free LiFePO₄ cell with the solid polymer electrolyte (SPE) delivers a discharge capacity of 127 mAh g⁻¹ at 25°C with a capacity retention of 87.5% after 500 cycles at 0.5°C (0.15 mA cm⁻²). Phase-field simulations and density functional theory calculations demonstrate that the negatively charged benzimidazole chains of PBI own superior affinity to lithium bis(trifluoromethanesulfonyl)imide (LiTFSI), and shares overlapping electron density with Li anode, giving rise to accelerated Li⁺ conduction at room temperature and uniform Li electrodeposition at the electrolyte/Li metal interface. The SPE is also flame-retardant since heat-resistant polytetrafluoroethylene and a dense, heat-blocking graphitized carbon layer are formed in intense heat through

Dongjiang Chen, Yuanpeng Liu, and Chuan Xia have contributed equally to this study.

This is an open access article under the terms of the Creative Commons Attribution License, which permits use, distribution and reproduction in any medium, provided the original work is properly cited.

© 2021 The Authors. *InfoMat* published by UESTC and John Wiley & Sons Australia, Ltd.

dehydrogenation/fluorination of PVDF under the catalysis of Lewis base imidazole rings and the decomposition of benzimidazole rings in PBI. No such fire-resistant mechanism is ever reported in conventional electrolytes.

KEYWORDS

flame-retardant properties, Li metal, polybenzimidazole, solid polymer electrolyte, uniform Li deposition

1 | INTRODUCTION

The surging demand for high-energy-density batteries urges the utilization of lithium (Li) metal anode due to its high theoretical capacity (3860 mAh g^{-1}), favorable gravimetric density (0.534 g cm^{-3}), and negative electrochemical potential (-3.04 V vs normal hydrogen electrode).¹ Nevertheless, highly reactive Li metal and electrolyte decomposition at high voltage cause safety concerns due to notorious dendrite growth and intense heat released from the exothermic reaction between Li anode and liquid electrolytes,² leading to two major research efforts in the field of Li metal batteries (LMBs), namely suppression on Li dendrite formation and enhancement on physicochemical properties of electrolytes.

Extensive research efforts have been centered on improving the applicability of the Li anode in liquid LMBs. For instance, Li anode architecture design, including constructing 2D/3D Li anode skeleton³ and utilizing aprotic bimetallic Li-Na alloy,⁴ effectively suppresses Li protuberance by accommodating charge distribution. Liquid electrolyte engineering based on organic trisaminocyclopropenium cations⁵ and *N,N*-dimethylacetamide additives⁶ can inhibit dendrite growth through electrostatic shielding effect and reconstruction of the Li^+ solvation structure. Constructing an artificial solid electrolyte interface (SEI) with thermoplastic polyurethane,⁷ tetraethyl orthosilicate,⁸ and hydrophobic SiO_2 nanoparticles coupled with CF_3SO_3^- functional group,⁹ has been proposed to stabilize Li interface without dendrite growth. Compositing monolayer separators with organosulfur compounds to build a resilient SEI is also proposed to attenuate ionic concentration gradient and eliminate dendrite growth.¹⁰ In addition, protective coating layers¹¹ and multilayer functional separators¹² have been realized to avoid the perturbation in the Li deposition process. Nonetheless, all these aforementioned strategies are based on the utilization of volatile, inflammable liquid electrolytes, still posing potential threats to safe operation of LMBs.

Solid polymer electrolytes (SPEs) with increased thermostability have been proposed as alternatives to liquid electrolytes.^{13,14} Polyethylene oxide (PEO) polymer enables

Li^+ transport through segmental motion and is frequently exploited due to low cost and lightweight.¹⁵ However, highly crystalline PEO requires a high operating temperature ($\sim 60^\circ\text{C}$) to agitate chain motion which sacrifices its mechanical strength.¹⁶ Poly(vinylidene fluoride) (PVDF), a polar and semicrystalline polymer with small van der Waals radius (1.32 \AA) fluorine atoms and robust C—F bond (485 kJ mol^{-1}), owns low surface energy, high dielectric constant and inertness to oxidation, all of which are essential for SPEs.^{17,18} Based on this conception, PEO and PVDF polymer blend with increased amorphous region was studied to enhance room-temperature conductivity.¹⁹ Nevertheless, the low melting point of PEO owing to feeble intermolecular van der Waals forces prevents it from operation above 90°C .²⁰ High melting point polymers, such as poly(methylmethacrylate) (PMMA)²¹ and poly(acrylonitrile) (PAN),²² own improved thermostability to resist dimensional deformation, but those polymer additives are flammable due to the easy cleavage of C—C bonds.²³

In this report, we design a flame-retardant SPE by incorporating fire-resistant polybenzimidazole (PBI) to reinforce α -phase PVDF matrix. The multiple proton donor sites ($-\text{NH}-$) of PBI form dense hydrogen bonds (-0.26 eV , $5.4 \times 10^{-3} \text{ mol g}^{-1}$) with PVDF, decreasing its dimensional shrinkage by 40% at 300°C . Nuclear magnetic resonance (NMR) and x-ray photoelectron spectroscopy (XPS) of the SPE combustion residues and emissions confirm that partial $-\text{CH}_2-\text{CF}_2-$ structure in PVDF is converted to nonflammable $-\text{CF}_2-\text{CF}_2-$ segments of polytetrafluoroethylene (PTFE) under the catalysis of imidazole rings of PBI in the burning process. PBI also forms a high-graphitization residual carbon layer on the SPE surface to block heat and O_2 for extinguishing. Density functional theory (DFT) calculations verify that negatively charged PBI owns a large adsorption energy with lithium bis(trifluoromethanesulfonyl)imide (LiTFSI), and shares an overlapping electron density with the Li anode, giving rise to expedited Li^+ conduction at room temperature and a homogeneous electric field to yield a dendrite-free Li anode. A LiFePO_4 cell with the PBI/PVDF/LiTFSI SPE delivers a 127 mAh g^{-1} discharge capacity at 25°C with an 87.5% capacity retention after 500 cycles at 0.5°C (0.15 mA cm^{-2}).

2 | RESULTS AND DISCUSSION

2.1 | Design concepts and characterizations of PBI electrolyte

A PBI molecular monomer owns a five-membered aromatic heterocycle with two intermediate nitrogen atoms (imidazole) and a benzene ring in the polymer backbone (Figure 1C). The thermostability of a polymer depends primarily on the strength of chemical bonds to endure chemical structure change at extreme temperatures.²⁴

The bond energy of delocalized π -bond (5.37 eV), C=C (6.59 eV), and C=N (6.37 eV) bonds in the benzimidazole ring is above that of the C—C bond (3.69 eV) in the PVDF backbone, leading to better thermal stability as compared with PVDF. Electrostatic potential analysis illustrates that the benzimidazole chain owns a negatively charged surface to coordinate with Li^+ and improve Li^+ dissociation,²⁵ while the negative charges in PVDF reside on fluorine atoms (Figure 1B–D). Both the proton acceptor ($-\text{N}=\text{N}-$) and donor ($-\text{NH}-$) groups in the imidazole ring contribute to robust intramolecular hydrogen bonds and

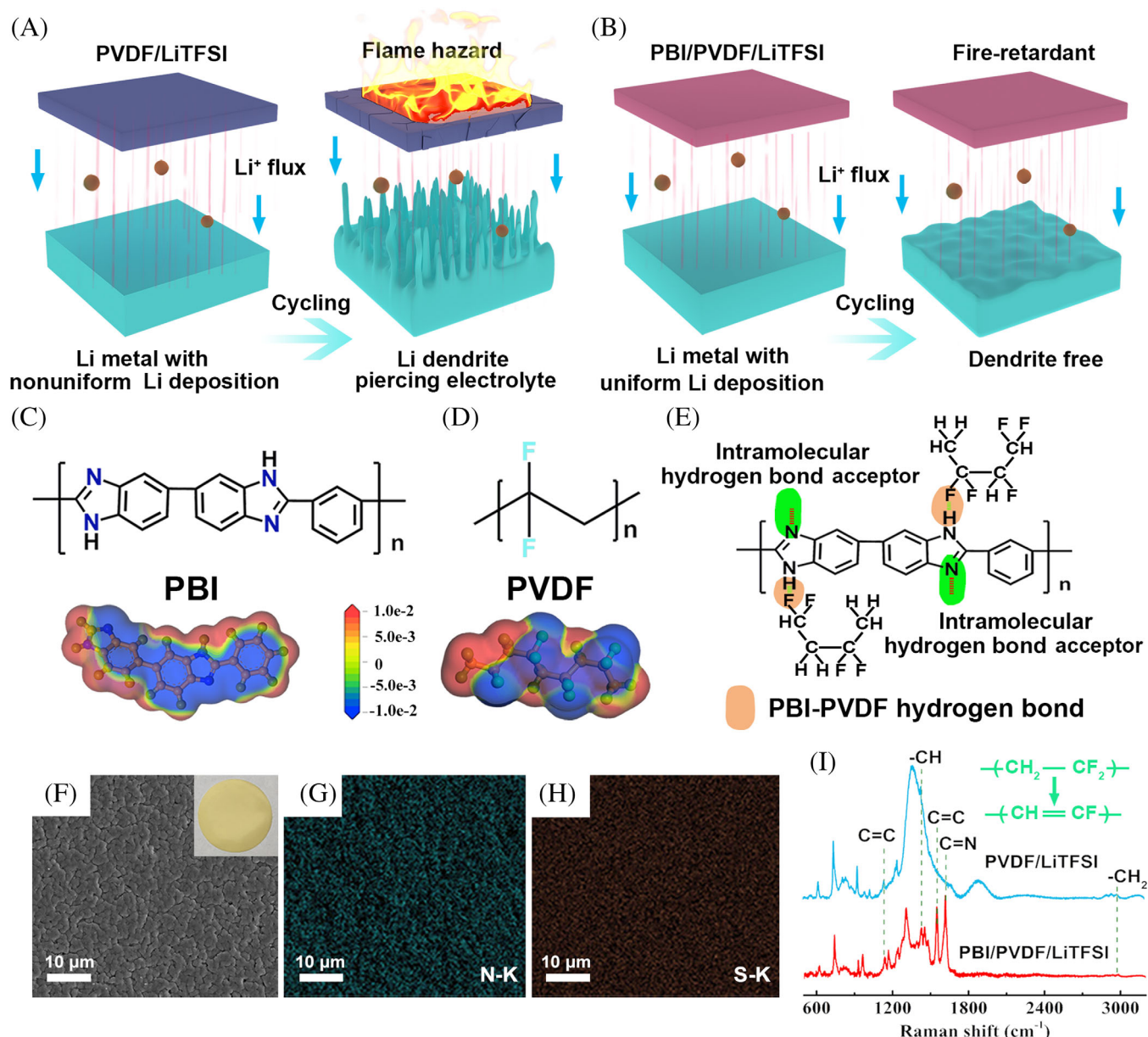


FIGURE 1 Molecular structures and design concepts of PBI/PVDF/LiTFSI SPE. Schematics of lithium-ion electrodeposition behaviors based on (A) PVDF/LiTFSI and (B) PBI/PVDF/LiTFSI. The molecular structures and electrostatic potentials of (C) PBI and (D) PVDF. (E) Schematic diagram of hydrogen-bonding sites in PBI. (F) SEM and optical images of PBI/PVDF/LiTFSI. Elemental mapping images of (G) N and (H) S in PBI/PVDF/LiTFSI. (I) Raman spectra of PVDF/LiTFSI and PBI/PVDF/LiTFSI with a 785 nm laser

intermolecular hydrogen bonds with PVDF through $\text{—NH}\cdots\text{F—C—}$ bonding (Figure 1E).²⁶ The interaction between PBI and PVDF is further confirmed with DFT calculations, as shown in Figure S1. The adsorption energy between PBI and PVDF is -0.26 eV, which is comparable to the hydrogen bond.

The thickness of the SPEs is $50\text{ }\mu\text{m}$ (Figure S2B,C) and homogeneous distribution of PBI and lithium salts is demonstrated with N and S elements mapping in Figure 1G,H. As shown in Figure S2A, the images of scanning electron microscopy (SEM) show surficial cavities at the PVDF/LiTFSI SPE interface, which induces uneven lithium-ion distribution and dendrite growth at the SPE/Li anode interface (Figure 1A). In contrast, Figure 1F shows a compact and dense surface of PBI/PVDF/LiTFSI SPE due to the dense hydrogen bonds between PBI and PVDF (5.4×10^{-3} mol g^{-1} , calculation details in molecular dynamics simulations). Fourier transform infrared (FT-IR) spectroscopy of PBI confirms the characteristic peaks of in-plane C=N , in-plane C—H , and N—H wagging vibration at 1480 , 1227 , and 1184 cm^{-1} (Figure S3), respectively.^{27,28} For PVDF, the peaks at 488 , 766 , and 851 cm^{-1} are attributed to α -phase PVDF,²⁹ and the peaks at 766 and 851 cm^{-1} correspond to the bending and out-of-plane deformation of CF_2 and C—H bonds, respectively. The composite of the PBI and PVDF verifies all characteristic bonds of both. As shown in Figure 1I, Raman spectra show the C=C and C=N vibrations of the benzimidazole ring at 1546 and 1616 cm^{-1} after the addition of PBI.³⁰ The peak intensity of the —CH_2 group at 2980 cm^{-1} in PVDF significantly decreases and those of —CH (1432 cm^{-1}) and C=C (1132 cm^{-1}) increase with PBI incorporation. This is because imidazole rings act as Lewis bases to donate lone pair electrons and induce partial deprotonation of —CH_2 in PVDF to form C=C bonds.³¹ Figure S4 shows that the key performance of PBI/PVDF/LiTFSI, including flame-retardant capability, operational temperature range, cell capacity, cycle life, and dendrite suppression, outperforms the state-of-the-art composite polymer/polymer solid electrolytes.^{32,33}

2.2 | Binary PBI/PVDF SPE for high-performance batteries

The electrochemical window of PBI is investigated by calculating the energy levels of the lowest unoccupied molecular orbital (LUMO) and the highest occupied molecular orbital (HOMO). Stable electrochemical operation requires a LUMO value above -3.96 eV and a HOMO value below -5.36 eV (calculation details in Experiments section). As shown in Figure S5A, the HOMO and LUMO values are -5.44 and -1.82 eV,

respectively, suggesting that PBI is electrochemically stable in the redox reactions, which is consistent with the linear sweep voltammetry experimental results (Figure S5B). Figure S5C shows that the reduction process commences at 2.1 V for PVDF/LiTFSI, while it is extended to 1.8 V for PBI/PVDF/LiTFSI, indicating that the addition of PBI effectively improves the electrochemical stability of PVDF/LiTFSI in low potential. As shown in Figure 2A, cyclic voltammetry (CV) shows much higher redox peaks for PBI/PVDF/LiTFSI as compared with those of PVDF/LiTFSI, indicating improved kinetics in electrochemical reactions. No redox peak shift is observed within the first three cycles for the cell with PBI/PVDF/LiTFSI SPE (Figure 2B), indicating a short cell stabilization time due to fast Li^+ transfer. As shown in Figure 2C, electrochemical impedance spectroscopy (EIS) shows that the PBI/PVDF/LiTFSI cell owns a much smaller semicircle diameter (R_{ct}) at the medium and high frequency region as compared with PVDF/LiTFSI cell, which is attributed to the lower charge transfer resistance at the PBI/Li metal interface. The Li^+ transference number (Figures 2D and S6) of PBI/PVDF/LiTFSI is 0.49 , higher than that of PVDF/LiTFSI (0.37), which is attributed to improved Li^+ dissociation from LiTFSI and impeded movement of TFSI $^-$ by the electron-enriched benzimidazole chains featured with negatively charged surfaces. By contrast, the dipoles (C—H and C—F) of α -PVDF, the most thermally stable PVDF at room temperature, are antiparalleled with TGTG' (T-trans, G- gauche $^+$, G'-gauche $^-$) dihedral conformation, leading to a nonpolar molecular structure, which is ineffective in improving the Li^+ transference number.³⁴ Symmetric Li/Li cells are tested at 0.025 – 0.2 mA cm^{-2} to evaluate dendrite suppression effects of various SPEs. Figure 2E shows a stable voltage profile for the PBI/PVDF/LiTFSI cell over 260 h. In contrast, the voltage polarization of the PVDF/LiTFSI cell is higher at all currents. Dramatical voltage fluctuation starts as the current density increases to 0.2 mA cm^{-2} and a short circuit occurs after 220 h. Since transient nonuniform protrusions could occur at a high current density due to fast Li^+ plating, the voltage fluctuation of the PBI/PVDF/LiTFSI cell is possibly due to lithium cracks, pulverization, and peeling off from the protrusions.^{35–37} As shown in Figure S7, a long-term (110 h) stable voltage profile is demonstrated with PBI/PVDF/LiTFSI at 0.2 mA cm^{-2} , two times longer than that of PVDF/LiTFSI (40 h). Figure 2F shows a higher ionic conductivity for the PBI/PVDF/LiTFSI SPE as compared with the PVDF/LiTFSI SPE. We further conduct high-temperature cycling to evaluate the thermal stability of the PBI-reinforced SPE. As shown in Figure 2G, the PVDF/LiTFSI cell shows a rapid capacity decrease as the temperature exceeds 75°C and stops working at 90°C . In comparison, the PBI/PVDF/LiTFSI

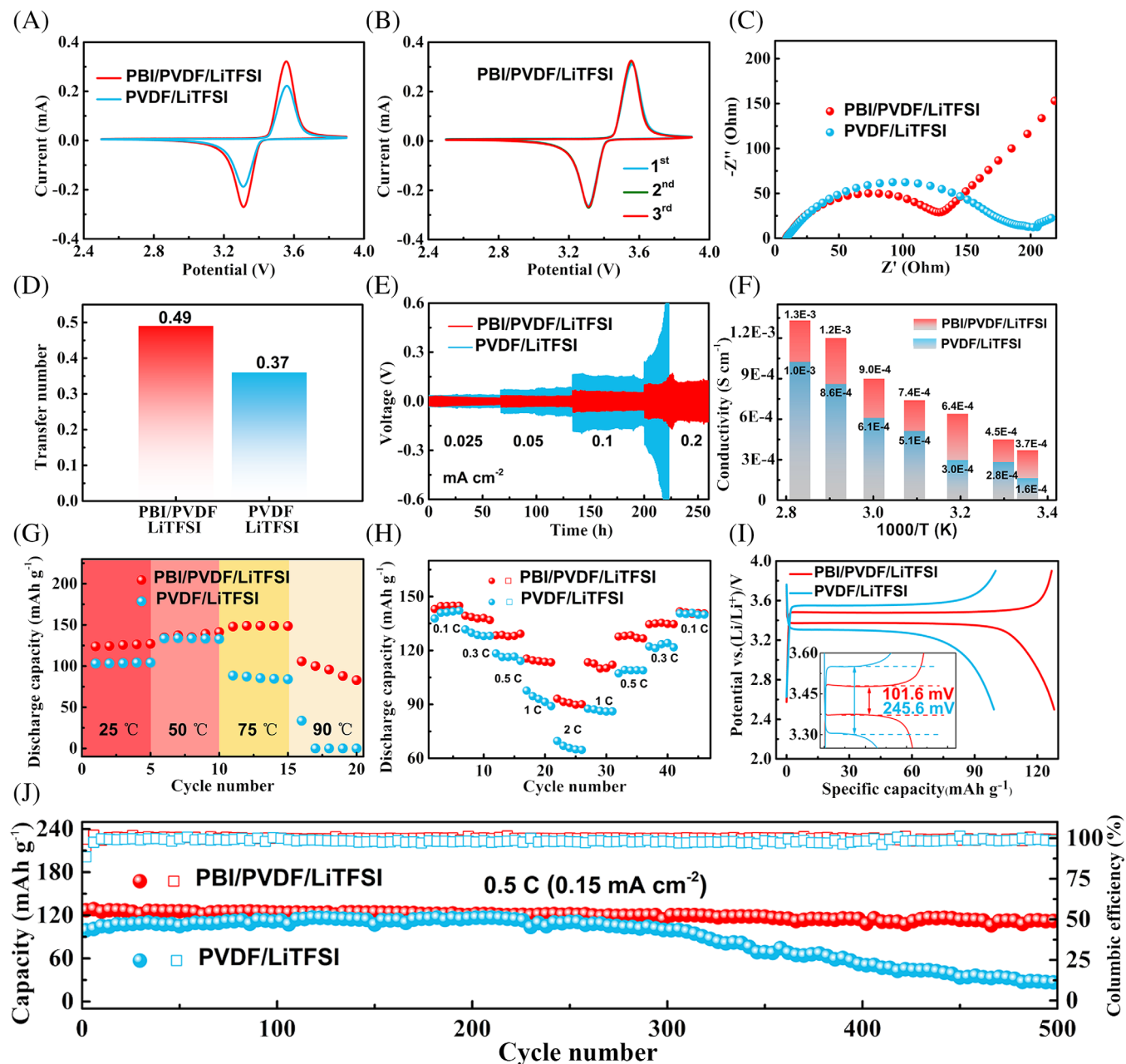


FIGURE 2 Electrochemical performance of batteries. (A) CV curves of PBI/PVDF/LiTFSI and PVDF/LiTFSI and (B) CV curves of PBI/PVDF/LiTFSI in the first three cycles scanning from 2.5 to 3.9 V at a rate of 0.5 mV s⁻¹. (C) EIS curves in the frequency range from 0.01 Hz to 1 MHz. (D) Li^+ ion transfer numbers, (E) cycling performance of symmetrical Li/Li cells, and (F) ionic conductivities based on PBI/PVDF/LiTFSI and PVDF/LiTFSI. (G) High-temperature cycling performance at 0.5°C and (H) rate performance of LiFePO₄/Li cells with PBI/PVDF/LiTFSI and PVDF/LiTFSI. (I) Charge/discharge profiles and (J) cycling performance of LiFePO₄/Li cells with PBI/PVDF/LiTFSI and PVDF/LiTFSI at 0.5°C

cell delivers a capacity of ~85 mAh g⁻¹ even at 90°C, demonstrating the much-enhanced thermal stability after the incorporation of PBI. As shown in Figure 2H, the PBI/PVDF/LiTFSI cell delivers discharge capacities of 143 mAh g⁻¹ at 0.1°C and 93 mAh g⁻¹ 2°C, while the PVDF/LiTFSI cell 138 mAh g⁻¹ at 0.1°C and 64 mAh g⁻¹ at 2°C, indicating significantly improved rate performances. Figure 2I shows that the voltage hysteresis of the

PBI/PVDF/LiTFSI cell (101.6 mV) is below that of the PVDF/LiTFSI cell (245.6 mV). As shown in Figure 2J, the PBI/PVDF/LiTFSI cell delivers a high discharge capacity of 127 mAh g⁻¹ at 0.5°C (0.15 mA cm⁻²) with an 87.5% capacity retention after 500 cycles (111.2 mAh g⁻¹). For comparison, the capacities of the PVDF/LiTFSI cell significantly decrease after ~300 cycles due to the large interfacial resistance and inferior thermal stability. Such

advantageous performance of PBI/PVDF/LiTFSI SPE is also demonstrated with high-loading cathodes (Figure S8).

The effects of the benzimidazole functional groups with various mass fractions in the composite solid electrolyte are investigated. Prolonged cycling life and improved capacity are observed for the PBI/PVDF/LiTFSI cell as compared with the PVDF/LiTFSI cell (Figure S9). The cell capacity increases with increasing PBI content from 5% to 8% since the hydrogen bonds between PBI and PVDF reinforce the structure, stabilize the SPE/Li anode interphase, and accelerate Li-ion transport. However, excessive PBI (8%–10%) leads to capacity decay because the rigid PBI chains impair the motion of PVDF chains. We further fabricate a PBI/LiTFSI SPE without PVDF. Robust intramolecular hydrogen bonds between proton acceptor ($-\text{N}=\text{}$) and donor

($-\text{NH}-$) groups in the imidazole ring form a rigid chain structure in which C—C bonds on the polymer backbone fail to rotate and oscillate to transport Li^+ . In addition, high glass phase transition temperature of PBI (425°C) prevents the chain from swinging effectively below 425°C . Consequently, the cell assembled with PBI/LiTFSI fails to run, demonstrating that PBI alone cannot be used as a SPE.

2.3 | Inhibition mechanisms of Li dendrite growth

DFT calculations are carried out to understand the Li transfer and plating behaviors. Figure S10 shows that the adsorption energy between LiTFSI and PBI (-1.49 eV) is far beyond that between LiTFSI and PVDF (-0.86 eV),

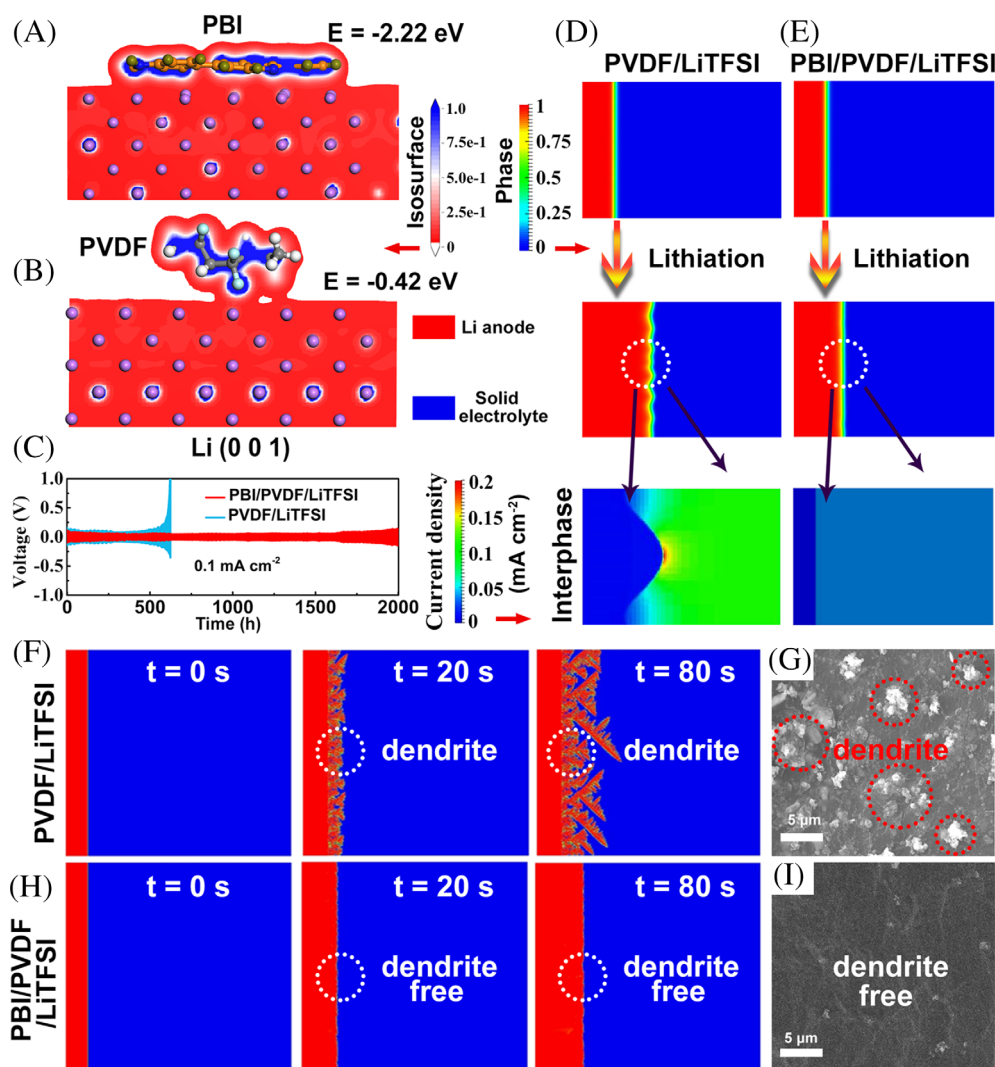


FIGURE 3 DFT calculations and phase-field simulations at interfaces. Electron density maps of (A) PBI and (B) PVDF on the Li (001) surface, respectively. (C) Long-term cycling of symmetrical Li/Li cells with PBI/PVDF/LiTFSI and PVDF/LiTFSI at 0.1 mA cm^{-2} . Phase-field simulations of current evolutions of (D) PVDF/LiTFSI and (E) PBI/PVDF/LiTFSI. Phase-field simulations of morphology evolutions of (F) PVDF/LiTFSI and (H) PBI/PVDF/LiTFSI. SEM images of Li metal with (G) PVDF/LiTFSI and (I) PBI/PVDF/LiTFSI after cycles

allowing for stronger combination of LiTFSI in binary PBI/PVDF SPE. As shown in Figure S11, the adsorption energy of Li^+ on PBI is -2.8 eV, which is significantly higher than that on PVDF (-1.98 eV) and the Li (0 0 1) surface (-1.37 eV), showing that Li^+ ions are preferentially adsorbed on PBI rather than the Li metal surface and PVDF. As shown in Figure 3A, the rigid chain structure of PBI prevents it from rotating and thus shows a planar conformation on the Li (0 0 1) surface, both sharing uniform electron distribution, which uniformizes the Li^+ concentration at the interface (Figure S12A). The higher adsorption energy of Li (0 0 1)/PBI (-2.22 eV) compared with Li (0 0 1)/PVDF (-0.42 eV) verifies increased affinity between the PBI/PVDF SPE and Li metal. The robust adsorption of PBI with both LiTFSI and Li metal expedites Li^+ conduction, accounting for the as-obtained improved Li^+ conductivity at room temperature. As PVDF is on the Li (0 0 1) surface, the electronegativity difference between H (2.20) in C—H dipole and F (3.98) in C—F dipole causes the C—C bond on the backbone to rotate where C—F bond is more prominent and closer to the surface of Li metal. The partially overlapping charge density between PVDF and Li (0 0 1) indicates that Li^+ ions tend to accumulate to form dendrites at the Li metal surface due to the uneven electric field on the Li anode surface (Figures 3B and S12B). During the following Li plating/stripping processes, a solid electrolyte interphase (SEI) consisting of LiF is formed on Li metal surface due to the decomposition of LiTFSI,³⁸ as confirmed with XPS and FT-IR (Figure S13A,B).^{39,40} As shown in Figure S13C, the uniform electron distribution between LiF (1 0 0) and PBI indicates that PBI with planar configuration also favors homogeneous Li deposition at SEI, delivering a long-term stable voltage profile over 2000 h at a current density of 0.1 mA cm^{-2} (Figure 3C), which is over three times longer than that of the PVDF/LiTFSI SPE (620 h).

Phase-field simulations are employed to numerically study the electric-field distribution at the SPEs/Li metal interface, as shown in Figure 3D,E. Parameter $\xi = 0$ (blue region) denotes the solid electrolyte phase, and $\xi = 1$ (red region) denotes the lithium anode phase. The region between the blue and red zones represents their interface. After Li electroplating (Figure 3D), the PVDF/LiTFSI model shows needle-like protrusions at the SPE/Li metal interface. The current density at the top of the protuberance is up to 0.2 mA cm^{-2} , but only 0.05 mA cm^{-2} at the bottom. Based on the electrostatic potential equation (equation (S3) in the Supporting Information S1), the nonuniform protrusions lower the electric potential and accumulate Li ions at the top of the protrusions, aggravating the unevenness of ion distribution and leading to the growth of large Li dendrites. For PBI/PVDF/LiTFSI,

uniform interfacial current density (0.05 mA cm^{-2}) is observed on the Li metal surface. The uniform spatial-electric-field distribution demonstrates that the lithiophilic benzimidazole chain effectively suppresses lithium dendrite growth.

The surface morphologies of various SPEs after cycling are characterized to illustrate the theoretical simulations. As shown in Figure S14A, mossy-like dendrites are observed on the PVDF/LiTFSI SPE. In comparison, PBI/PVDF/LiTFSI SPE shows smooth and flat morphology (Figure S14B), further revealing that the incorporation of PBI in the solid electrolyte effectively stabilizes Li metal anode for uniform Li deposition (Figure 1B). The dendrite formation kinetics is further visualized with phase-field simulations. Li metal with PVDF/LiTFSI SPE exhibits obvious dendrite growth over time (Figure 3F and Video S1), which is consistent with the SEM image after Li deposition, showing rough surface with rough protrusions (Figure 3G). For comparison, the Li plating morphology in the PBI/PVDF/LiTFSI cell owns a smooth surface from both theoretical and experimental results (Figure 3H,I and Video S2), as attributed to the homogeneous spatial-electric-field distribution at the PBI/Li anode interphase. As shown in Figure S14C–I, the interface morphologies of PBI/LiTFSI SPE, PBI/PVDF, and Li anode show no difference after assembled in cells for 24 h, indicating that both PBI and PVDF are stable with Li metal.

2.4 | Superior thermostability of PBI/PVDF SPE with flame-retardant properties

To gain further insights into intermolecular interaction between PBI and PVDF, molecular dynamics (MD) simulations are performed. Figure 4A shows that the linear chains of pure PVDF disentangle and orient to the stretching direction under uniaxial tension, accounting for the weak van der Waals force in neighboring chains. A microscale void forms initially and propagates rapidly into a large crack, leading to a final rupture without pulling chains. With PBI (Figure 4B), intermolecular and intramolecular hydrogen bonds form between N—H (donors) and electronegative atoms N and F (acceptors). PBI serves as an “anchor” to twine the PVDF chains through physical crosslinks, dissipates energy by relaxing the stretched polymer chains, and, thus, effectively prevents the PVDF chain from sliding and unwinding even under an increased strain. The experimental strain–stress curves show that the PBI/PVDF/LiTFSI SPE owns better mechanical properties (5.3 MPa) in comparison with PVDF/LiTFSI SPE (4.8 MPa), which is consistent with theoretical MD simulations, as shown in Figure S15. We further construct a mathematical model to estimate the

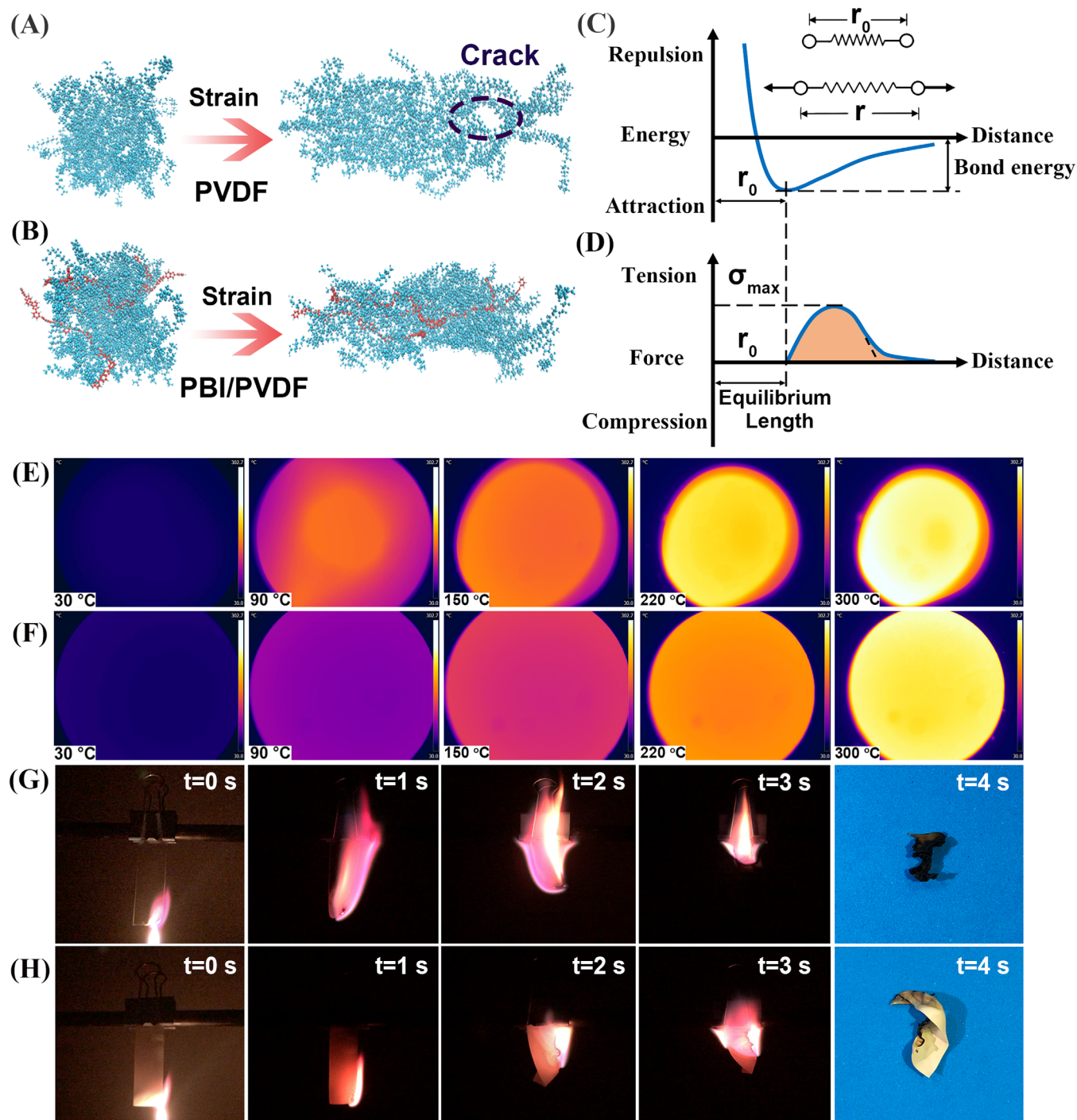


FIGURE 4 Mechanical strength and thermal stability. Molecular dynamics simulations of (A) PVDF and (B) PBI/PVDF under 170% tensile strain. (C) Interatomic potential energy and (D) interatomic forces as a function of separation distance. FLIR images of (E) PVDF/LiTFSI and (F) PBI/PVDF/LiTFSI from 30°C to 300°C. Optical photographs of the burning tests of (G) PVDF/LiTFSI and (H) PBI/PVDF/LiTFSI

strength of solid electrolytes. The solid electrolyte is assumed to be elastic and isotropic. The interatomic force and potential energy associated with the separation distance of the atoms are schematically shown in Figure 4C,D, respectively.

Based on the dependence of the stress upon the atomic displacement, we assume that the relationship between stress σ_s and the atomic separation distance from the equilibrium position x approximately follows a sine function:

$$\sigma_s = \sigma_{\max} \sin(2\pi x / \lambda) \quad (1)$$

where σ_{\max} is the maximum stress (theoretical strength) and λ is the wavelength of sine function. The Hooke's law gives the stress between two atoms:

$$\sigma_s = Ex / r_0 \quad (2)$$

where E is the Young's modulus of the electrolyte and r_0 is the equilibrium distance between pairs of atoms. Based on the Griffith's theory, the thermodynamics requires that the work to break bonds should be above the work to create a new surface, yielding:

$$\int_0^{\lambda/2} \sigma_{\max} \sin(2\pi x / \lambda) dx = G_{be} \quad (3)$$

where G_{be} is the bond energy. The integral leads to:

$$G_{be} = \lambda \sigma_{\max} / \pi \quad (4)$$

Combining Equations (1)–(4) yields:

$$E = \frac{2r_0 \sigma_{\max}^2}{G_{be}} \quad (5)$$

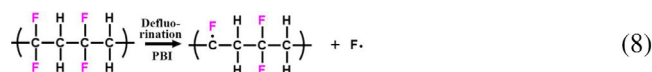
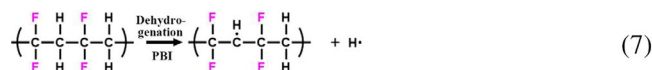
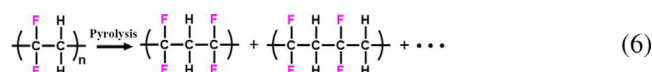
where σ_{\max} and r_0 are the theoretical strength and equilibrium distance between pairs of atoms, respectively. G_{be} and E are the bond energy and the Young's modulus of the solid electrolyte obtained from DFT calculations. We then analyze the failure modes of solid electrolytes by correlating strength and bond energy based on Equation (5). According to the estimated bond strength (Table. S1), the strength of hydrogen bond is ~ 4 times stronger than that of the van der Waals force, suggesting that introducing hydrogen bonds between the two polymer molecules is effective for enhancing the mechanical strength of PVDF/LiTFSI SPE.

Forward-looking infrared radiometer (FLIR) is employed to analyze the thermal stability of the SPEs. The conformation of PVDF/LiTFSI experiences severe deformation due to the accumulation of heat as the temperature is above 150°C (Figure 4E). For comparison, PBI/PVDF/LiTFSI exhibits a uniform thermal distribution as temperature increases from 30°C to 300°C. The thermal shrinkage of the PBI/PVDF/LiTFSI SPE is 29% at 300°C, which is much smaller as compared with PVDF/LiTFSI (49%, Figure 4F). The 40% reduction in thermal shrinkage demonstrates that heat transfers rapidly from the substrate to the PBI reinforced SPE surface without local heat accumulation. The flame-retardant

properties of the PBI/PVDF/LiTFSI SPE are investigated with igniting tests. Thermogravimetry analysis shows the inevitable existence of combustible plasticizer 1-methyl-2-pyrrolidinone in the PVDF matrix (Figure S16). As shown in Figure 4G and Video S3, the PVDF/LiTFSI SPE shows immediate shrinkage and complete combustion as exposed to fire, which carbonizes PVDF with the release of a huge amount of heat. Although PBI/PVDF/LiTFSI SPE is ignited at the initial stage, the flame is significantly weaker than that of PVDF/LiTFSI SPE and shows self-extinguishing properties, demonstrating the superior fire retarding capability (Figure 4H and Video S4).

2.5 | Evolution of binary PBI/PVDF SPE in fire

We simulate the PBI/PVDF architecture evolution in a high-temperature environment through Ab initio molecular dynamic (AIMD) calculations to evaluate the flame-retardant mechanism, as shown in Figure 5A. PVDF is pyrolyzed to a low-molecular-weight fluoropolymer at 200 fs (Equation (6)), accompanied with the formation of hydrogen radicals (H \cdot) and fluorine radicals (F \cdot) due to the C–H and C–F bonds breakage (Equations (7) and (8)).



As shown in Figure S17, the energy barrier for the C–H and C–F bond breakages in PVDF chain is 3.62 and 2.94 eV, respectively. After the addition of PBI, the energy barriers remarkably decrease to 2.55 and 1.65 eV. Since defluorination and formation of H \cdot are energetically favorable in the alkaline environment,⁴¹ we propose that the imidazole ring, acting as a Lewis base, catalyzes the dissociation of H and F atoms from the PVDF chain in fire, leading to formation of more H \cdot and F \cdot . Figure S18 shows that H \cdot reacts with oxygen (O $_2$) to form H $_2$ O through the intermediate state of oxyhydrogen radical (\cdot OH) in fire (Equations (9) and (10)).⁴² In addition, PVDF chain also readily forms HF molecules through dehydrofluorination (500 fs),⁴³ leading to the formation of C=C bond (Equation (11) and process 1 of Figure 5C).

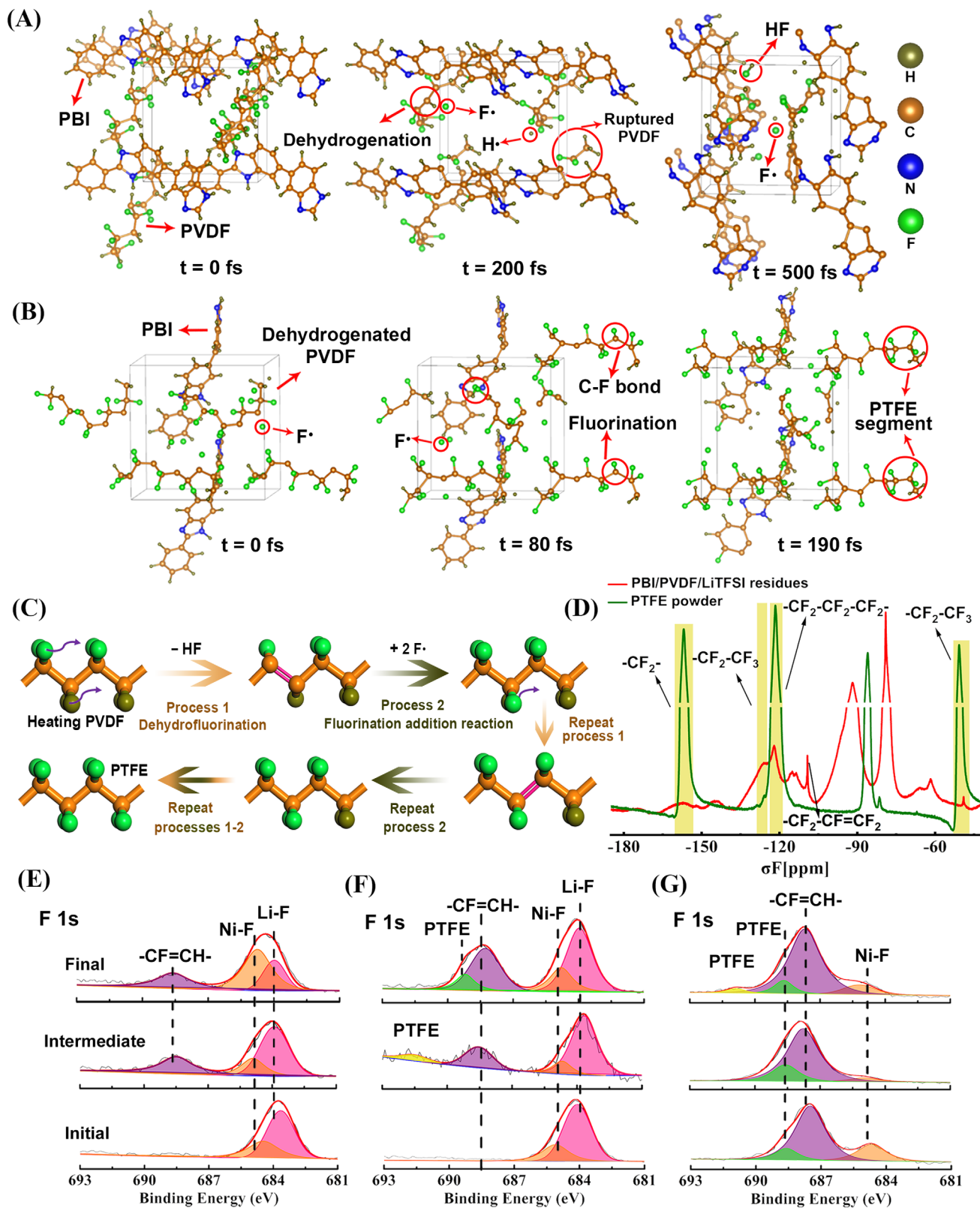
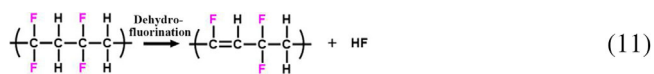
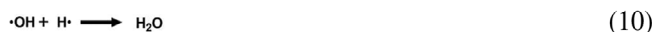
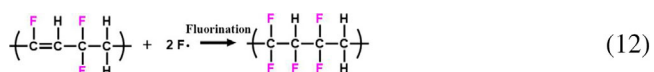


FIGURE 5 Theoretical and spectral analysis of combustion products and proposed fire-retardant mechanism. (A) AIMD simulations of the PBI/PVDF architecture variation and (B) the formation of PTFE. (C) Proposed fire-retardant mechanism of molecular structure evolution from PVDF to PTFE. (D) ^{19}F solid-state NMR spectra of the PBI/PVDF/LiTFSI residues after combustion and the PTFE powder. High-resolution XPS spectra of F 1s of (E) PVDF/LiTFSI, (F) PBI/PVDF/LiTFSI, and (G) PBI/PVDF combustion products at the initial, intermediate, and final states (from the bottom to the top)

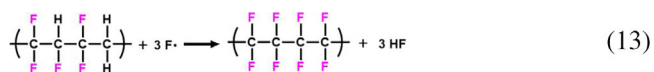
We hypothesize that the activated C=C bonds in the fluoropolymer chain react with free F[•] through nucleophilic addition reaction, giving rise to the PVDF structure



variation from $-\text{CF}=\text{CH}-\text{CF}_2-\text{CH}_2-$ to $-\text{CF}_2-\text{CHF}-\text{CF}_2-\text{CH}_2-$ (Equation (12) and process 2 of Figure 5C).



As the combustion continues, residual hydrogen atoms in the modified-PVDF structure are continuously replaced by fluorine atoms in repeated processes 1–2 (Equations (11)–(13) and Figure 5C), giving rise to the formation of the $-\text{CF}_2-\text{CF}_2-$ structure.



As shown in Figure 5B, F[•] and modified PVDF chain without H atoms are taken to simulate fluorination addition reaction with AIMD calculations. F[•] is attached to carbon atom in the polymer chain with the formation of C–F bond (80 fs), and $-\text{CF}_2-\text{CF}_2-$ structure is observed at 190 fs, confirming the formation of PTFE segments. Because high fluorine contents enable dramatically enhanced thermostability,^{17,18} the modified PVDF polymer with the $-\text{CF}_2-\text{CF}_2-$ structure owns fire self-extinguishing properties.

NMR is employed to verify experimentally the PVDF molecular structure variation by investigating the composition of the PBI/PVDF/LiTFSI residues after combustion. As shown in Figure 5D, the peaks located at -125.7 , -49.2 , and -122 ppm correspond to $-\text{CF}_2-\text{CF}_3$ and $-\text{CF}_2-\text{CF}_2-\text{CF}_2-$ fluorinated groups,⁴⁴ which is consistent with the results of the PTFE powders except the peak intensity, confirming the formation of $-\text{CF}_2-\text{CF}_2-$ segments in the modified PVDF molecular structure. Particularly, unsaturated C=C bond is observed at -109.2 ppm,⁴⁵ which supports our hypothesis that activated C=C bonds react with free F[•] through nucleophilic

addition reaction to form high fluorine contents segments ($-\text{CF}_2-\text{CF}_2-$) (process 2 of Figure 5C), confirming the self-extinguishing properties of PBI/PVDF/LiTFSI in fire. For comparison, no $-\text{CF}_2-\text{CF}_2-$ signal is detected for the residues of PVDF/LiTFSI, as shown in Figure S19. The dominant peaks at -91.4 and -78.7 ppm correspond to crystalline domain of PVDF (Figure S19), and the double peaks at -114.9 and -113.7 ppm are attributed to head-to-head PVDF units.⁴⁶ We further substitute PBI with polyimide (PI) that has a heterocyclic structure containing nitrogen atom to compound PVDF and investigate the residue composition after combustion. The NMR spectrum of PI/PVDF/LiTFSI shows no $-\text{CF}_2-\text{CF}_2-$ signal, confirming that imidazole ring of PBI catalyzes the dehydrogenation and fluorination of PVDF to form $-\text{CF}_2-\text{CF}_2-$ structure. Figure S19 shows that no $-\text{CF}_2-\text{CF}_2-$ signal is observed for the pristine PBI/PVDF/LiTFSI SPE before combustion, suggesting that the catalytic effect of PBI on PVDF to form PTFE segments is insignificant without fire. We further employ XPS to analyze the combustion products at various burning states. As shown in Figure 5E, at the initial burning state of PVDF/LiTFSI, the Ni–F signal (~ 685 eV) in F 1s spectra is attributed to the interaction between small resultant fluorochemical particulates, such as LiF (~ 684 eV), and Ni foam substrate during the combustion.⁴⁷ The peak at ~ 688.4 eV corresponds to $-\text{CF}=\text{CH}-$ group derived from $-\text{CF}_2-\text{CH}_2-$ in the PVDF chain after dehydrofluorination process,⁴⁸ which is consistent with the process 1 in the PTFE formation mechanism (Figure 5C). For PBI/PVDF/LiTFSI (Figure 5F), the $-\text{CF}_2-\text{CF}_2-$ signals protrude at 689.2 and 691.5 eV in F 1s spectra,⁴⁹ leading to superior heat-resistant and flame-retardant capability of PBI/PVDF/LiTFSI. The combustion product of PBI/PVDF polymer without LiTFSI is then studied. As shown in Figure 5G, although the various C–F bonds in F 1s spectra shift to lower binding energy, the $-\text{CF}_2$ signals of PTFE are prominent at 688.7 and 690.9 eV,^{50,51} confirming that partial PVDF is converted to fire-resistant PTFE segments through dehydrogenation and fluorination under the catalysis of imidazole rings in fire. In addition, we characterize the carbon residues of the SPEs after the burning test with Raman spectroscopy. As shown in Figure S20, the two dominant peaks at 1315 and 1585 cm^{-1} correspond to D band (amorphous carbon) and G band (graphitized carbon) of carbon, and the intensity ratio between D band and G band (I_G/I_D) represents the graphitization. For PBI/PVDF/LiTFSI, the value of I_G/I_D is 7.43, higher than that of PVDF/LiTFSI (4.87), indicating that the benzimidazole chain decomposes to highly graphitized carbon layer on PVDF to block heat and O₂.

3 | CONCLUSION

In summary, a PBI-reinforced solid polymeric electrolyte is developed. The binary SPE owns superior self-extinguishing properties by converting partial PVDF into fire-resistant PTFE segments in fire with PBI-catalyzed dehydrogenation and fluorination. The highly graphitized residual carbon layer on the SPE surface blocks heat and O₂ to further enhance the fire-extinguishing capability of the SPE. Theoretical simulations corroborate strong adsorption of lithiophilic PBI on both LiTFSI and the Li anode, which expedites Li⁺ conduction at room temperature and uniformizes the interfacial electric field for homogenous Li deposition, yielding a dendrite-free Li metal. Based on the proposed architecture, the all-solid-state Li metal batteries with PBI/PVDF/LiTFSI SPE delivers a high capacity of 111.2 mAh g⁻¹ after 500 cycles at 0.5°C (0.15 mA cm⁻² at 25°C).

ACKNOWLEDGMENTS

The work was supported by the Fundamental Research Funds for the Chinese Central Universities (Grant No. ZYGX2015Z003), the Science & Technology Support Funds of Sichuan Province (Grant No. 2016GZ0151), the Natural Science Foundation of China (Grant No. 51972043), and the Applied Fundamental Research Fund of Sichuan Province (Grant No. 2019YJ0169).

CONFLICT OF INTEREST

The authors declare no conflict of interest.

ORCID

Weidong He  <https://orcid.org/0000-0001-8242-2888>

REFERENCES

- Zheng J, Engelhard MH, Mei D, et al. Electrolyte additive enabled fast charging and stable cycling lithium metal batteries. *Nat Energy*. 2017;2(3):1-8.
- Yu Z, Wang H, Kong X, et al. Molecular design for electrolyte solvents enabling energy-dense and long-cycling lithium metal batteries. *Nat Energy*. 2020;5(7):526-533.
- Wu C, Huang H, Lu W, et al. Mg doped Li-LiB alloy with in situ formed lithiophilic LiB skeleton for lithium metal batteries. *Adv Sci*. 2020;7:1902643.
- Ma J-L, Meng F-L, Yu Y, et al. Prevention of dendrite growth and volume expansion to give high-performance aprotic bimetallic Li-Na alloy-O₂ batteries. *Nat Chem*. 2019;11(1):64-70.
- Ji W, Huang H, Zheng D, et al. A redox-active organic cation for safer metallic lithium-based batteries. *Energy Storage Mater*. 2020;32:185-190.
- Yu Y, Huang G, Du J-Y, et al. A renaissance of N,N-dimethylacetamide-based electrolytes to promote the cycling stability of Li-O₂ batteries. *Energy Environ Sci*. 2020;13(9):3075-3081.
- Liu T, Feng X-L, Jin X, et al. Protecting the lithium metal anode for a safe flexible lithium-air battery in ambient air. *Angew Chem Int Ed*. 2019;58(50):18240-18245.
- Yu Y, Yin Y-B, Ma J-L, et al. Designing a self-healing protective film on a lithium metal anode for long-cycle-life lithium-oxygen batteries. *Energy Storage Mater*. 2019;18:382-388.
- Yu Y, Zhang X-B. In situ coupling of colloidal silica and Li salt anion toward stable Li anode for long-cycle-life Li-O₂ batteries. *Matter*. 2019;1(4):881-892.
- Boateng B, Han Y, Zhen C, et al. Organosulfur compounds enable uniform lithium plating and long-term battery cycling stability. *Nano Lett*. 2020;20(4):2594-2601.
- Liu W, Lin D, Pei A, Cui Y. Stabilizing lithium metal anodes by uniform Li-ion flux distribution in nanochannel confinement. *J Am Chem Soc*. 2016;138(47):15443-15450.
- Liu K, Zhuo D, Lee H-W, et al. Extending the life of lithium-based rechargeable batteries by reaction of lithium dendrites with a novel silica nanoparticle sandwiched separator. *Adv Mater*. 2017;29(4):1603987.
- Jiang T, He P, Wang G, Shen Y, Nan C-W, Fan L-Z. Solvent-free synthesis of thin, flexible, nonflammable garnet-based composite solid electrolyte for all-solid-state lithium batteries. *Adv Energy Mater*. 2020;10(12):1903376.
- Wang J, Huang G, Chen K, Zhang X-B. An adjustable-porosity plastic crystal electrolyte enables high-performance all-solid-state lithium-oxygen batteries. *Angew Chem Int Ed*. 2020;59(24):9382-9387.
- Chen L, Li Y, Li S-P, Fan L-Z, Nan C-W, Goodenough JB. PEO/garnet composite electrolytes for solid-state lithium batteries: from "ceramic-in-polymer" to "polymer-in-ceramic". *Nano Energy*. 2018;46:176-184.
- Zhou F, Li Z, Lu Y-Y, et al. Diatomite derived hierarchical hybrid anode for high performance all-solid-state lithium metal batteries. *Nat Commun*. 2019;10(1):2482.
- Ameduri B. From vinylidene fluoride (VDF) to the applications of VDF-containing polymers and copolymers: recent developments and future trends. *Chem Rev*. 2009;109(12):6632-6686.
- Hu J, He P, Zhang B, Wang B, Fan L-Z. Porous film host-derived 3D composite polymer electrolyte for high-voltage solid state lithium batteries. *Energy Storage Mater*. 2020;26:283-289.
- Dhatarwal P, Sengwa RJ. Impact of PVDF/PEO blend composition on the β -phase crystallization and dielectric properties of silica nanoparticles incorporated polymer nanocomposites. *J Polym Res*. 2019;26(8):196.
- Nagle JF, Gujrati PD, Goldstein M. Towards better theories of polymer melting. *J Phys Chem*. 1984;88(20):4599-4608.
- Rajendran S, Mahendran O, Mahalingam T. Thermal and ionic conductivity studies of plasticized PMMA/PVdF blend polymer electrolytes. *Eur Polym J*. 2002;38(1):49-55.
- Gopalan AI, Santhosh P, Manesh KM, et al. Development of electrospun PVDF-PAN membrane-based polymer electrolytes for lithium batteries. *J Membr Sci*. 2008;325(2):683-690.
- Plawsky JL, Wang F, Gill WN. Kinetic model for the pyrolysis of polysiloxane polymers to ceramic composites. *AIChE J*. 2002;48(10):2315-2323.
- Korshak VV, Vinogradova SV. Dependence of thermal stability of polymers on their chemical structure. *Russ Chem Rev*. 1968;37(11):885-906.
- Wang J, He Y, Wu Q, et al. A facile non-solvent induced phase separation process for preparation of highly porous polybenzimidazole separator for lithium metal battery application. *Sci Rep*. 2019;9:19320.

26. Maity N, Mandal A, Roy K, Nandi AK. Physical and dielectric properties of poly(vinylidene fluoride)/polybenzimidazole functionalized graphene nanocomposites. *J Polym Sci B*. 2018;57(4):189-201.
27. Sheng L, Xu H, Guo X, Fang J, Fang L, Yin J. Synthesis and properties of novel sulfonated polybenzimidazoles from disodium 4,6-bis(4-carboxyphenoxy)benzene-1,3-disulfonate. *J Power Sources*. 2011;196(6):3039-3047.
28. Asensio JA, Borr s S, G mez-Romero P. Proton-conducting polymers based on benzimidazoles and sulfonated benzimidazoles. *J Polym Sci A Polym Chem*. 2002;40(21):3703-3710.
29. Bormashenko Y, Pogreb R, Stanevsky O, Bormashenko E. Vibrational spectrum of PVDF and its interpretation. *Polym Test*. 2004;23(7):791-796.
30. Quartarone E, Magistris A, Mustarelli P, et al. Pyridine-based PBI composite membranes for PEMFCs. *Fuel Cells*. 2009;9(4):349-355.
31. Zhang X, Liu T, Zhang S, et al. Synergistic coupling between $\text{Li}_{6.75}\text{La}_3\text{Zr}_{1.75}\text{Ta}_{0.25}\text{O}_{12}$ and poly(vinylidene fluoride) induces high ionic conductivity, mechanical strength, and thermal stability of solid composite electrolytes. *J Am Chem Soc*. 2017;139(39):13779-13785.
32. Wan J, Xie J, Kong X, et al. Ultrathin, flexible, solid polymer composite electrolyte enabled with aligned nanoporous host for lithium batteries. *Nat Nanotechnol*. 2019;14(7):705-711.
33. Zhang J, Zhao J, Yue L, et al. Safety-reinforced poly(propylene carbonate)-based all-solid-state polymer electrolyte for ambient-temperature solid polymer lithium batteries. *Adv Energy Mater*. 2015;5(24):1501082.
34. Pan H, Na B, Lv R, Li C, Zhu J, Yu Z. Polar phase formation in poly(vinylidene fluoride) induced by melt annealing. *J Polym Sci B*. 2012;50(20):1433-1437.
35. Chen R, Li Q, Yu X, Chen L, Li H. Approaching practically accessible solid-state batteries: stability issues related to solid electrolytes and interfaces. *Chem Rev*. 2020;120(14):6820-6877.
36. Dai H, Xi K, Liu X, Lai C, Zhang S. Cationic surfactant-based electrolyte additives for uniform lithium deposition via lithiophobic repulsion mechanisms. *J Am Chem Soc*. 2018;140(50):17515-17521.
37. He Y, Chang Z, Wu S, et al. Simultaneously inhibiting lithium dendrites growth and polysulfides shuttle by a flexible MOF-based membrane in Li-S batteries. *Adv Energy Mater*. 2018;8(34):1802130.
38. Cai D, Wang D, Chen Y, et al. A highly ion-conductive three-dimensional LLZAO-PEO/LiTFSI solid electrolyte for high-performance solid-state batteries. *Chem Eng J*. 2020;394:124993.
39. Hedderich HG, Frum CI RE Jr, Bernath PF. The infrared emission spectra of LiF and HF. *Can J Chem*. 1991;69(11):1659-1671.
40. Winie T, Arof AK. FT-IR studies on interactions among components in hexanoyl chitosan-based polymer electrolytes. *Spectrochim Acta A*. 2006;63(3):677-684.
41. Zhao X, Song L, Fu J, Tang P, Liu F. Experimental and DFT investigation of surface degradation of polyvinylidene fluoride membrane in alkaline solution. *Surf Sci*. 2011;605(11):1005-1015.
42. Li J, Zhao Z, Kazakov A, Dryer FL. An updated comprehensive kinetic model of hydrogen combustion. *Int J Chem Kinet*. 2004;36(10):566-575.
43. Liu F, Hashim NA, Liu Y, Abed MRM, Li K. Progress in the production and modification of PVDF membranes. *J Membr Sci*. 2011;375(1):1-27.
44. Lappan U, Fuchs B, Ge  ler U, Scheler U, Lunkwitz K. Number-average molecular weight of radiation-degraded poly(tetrafluoroethylene). An end group analysis based on solid-state NMR and IR spectroscopy. *Polymer*. 2002;43(16):4325-4330.
45. Katoh E, Sugimoto H, Kita Y, Ando I. Structures of polytetrafluoroethylene oligomers as studied by high-resolution solid-state ^{19}F NMR and their properties. *J Mol Struct*. 1995;355(1):21-26.
46. Holstein P, Scheler U, Harris RK. Semicrystallinity and polymorphism in PVDF: a solid-state ^{19}F NMR investigation. *Polymer*. 1998;39(20):4937-4941.
47. Tasaka A, Morimoto E, Mimoto A, Inoue A, Inaba M. Measurement and thermodynamic analysis of NiF_2/Ni electrode potential in a dehydrated melt of $\text{NH}_4\text{F}_2\cdot\text{HF}$. *ECS Trans*. 2007;3(35):529-542.
48. Feng K, Tang B, Wu P. Ammonia-assisted dehydrofluorination between PVDF and Nafion for highly selective and low-cost proton exchange membranes: a possible way to further strengthen the commercialization of Nafion. *J Mater Chem A*. 2015;3(24):12609-12615.
49. Gu  guen A, Nov  k P, Berg EJ. XPS study of the interface evolution of carbonaceous electrodes for Li-O_2 batteries during the 1st cycle. *J Electrochem Soc*. 2016;163(13):A2545-A2550.
50. Vasil'kov AY, Suzdalev IP, Maksimov YV, et al. Fibroporous polytetrafluoroethylene modified with iron nanoparticles: structure and electronic and magnetic properties. *Russ J Phys Chem A*. 2013;87(6):985-991.
51. Nasef MM, Saidi H, Nor HM, Yarmo MA. XPS studies of radiation grafted PTFE-g-polystyrene sulfonic acid membranes. *J Appl Polym Sci*. 2000;76(3):336-349.

SUPPORTING INFORMATION

Additional supporting information may be found in the online version of the article at the publisher's website.

How to cite this article: Chen D, Liu Y, Xia C, et al. Polybenzimidazole functionalized electrolyte with Li-wetting and self-fluorination functionalities for practical Li metal batteries. *InfoMat*. 2021;1-13. doi:10.1002/inf2.12247